Thin liquid films down a vertical microfiber: Effect of curvature elasticity

Weiyang Jiang and Zijing Ding*
School of Energy Science and Engineering, Harbin Institute of Technology, Harbin, China

(Received 4 October 2021; accepted 23 February 2022; published 15 March 2022)

In this paper, we use a long-wave model to examine how the curvature elasticity modifies the famous Plateau-Rayleigh mechanism and the formation of viscous beads on a vertically placed fiber. By blending the analyses of linear stability, weakly nonlinear stability, exact nonlinear solutions, and numerical simulations, the effects of spontaneous curvature, surface bending rigidity, Gaussian curvature, and Van der Waals forces on the Plateau-Rayleigh mechanism and breakup of the liquid film are examined. The spontaneous curvature and surface bending rigidity are stabilizing the interface, which can reduce the amplitude and wave speed of nonlinear traveling waves and retard the breakup of film caused by Van der Waals attractions. However, the Gaussian curvature effect reinforces the Plateau-Rayleigh mechanism, which accelerates the rupture of film.

DOI: 10.1103/PhysRevE.105.035104

I. INTRODUCTION

Liquid films coating a thin vertically placed fiber are widely encountered in nature and industrial applications, e.g., viscous beads on spider silk, water collection, desalination, and manufacture of nanofibers [1–3]. The gravity-surface-tension driven flow exhibits rich interesting dynamical phenomena, such as organized bead trains and complex interactions between multiscale beads [4], which have attracted much attention in the past decade. Many of these studies were conducted in complicated situations, e.g., with an applied electric field, temperature field, or flows on fibers with microstructured surfaces, aiming at controlling the Plateau-Rayleigh mechanism and pattern formation [5–8].

The experimental work of liquid films coating a cylinder was pioneered by Quéré [9], who found that a large droplet, formed from the merging of small beads, will appear quickly when the film is thick, while droplet formation will be arrested by the mean flow when the film is thin. For thin liquid film flows, simple models based on the long-wave assumption were used to examine the instability phenomenon caused by the surface tension, which showed that the azimuthal curvature is responsible for the droplet formation and breakup of films [10–13]. Recently, more interest has been concentrated on thick film flows, which showed more complicated dynamics than thin liquid film flow. In thick film, often thicker than the fiber, the flow exhibits different patterns that depend on the flow rates. Kliakhandler *et al.* [4] reported three different flow patterns, labeled regimes "a," "b," and "c" in the experiments. In flow regime "a," large and steadily moving droplets are separated by thin and long films. Flow regime "b" resembles a necklace structure. Flow regime "c" is an oscillatory state, in which a large droplet coexists with several tiny droplets. An interesting phenomenon is that the complicated interactions between the large droplet and small droplets result in the exact relative periodic orbit [14]. Modeling of the thick film flow is more challenging than that in the thin film flow case. Craster and Matar derived an asymptotic model for when the flow rate is low, i.e., when the inertial effect is not important, and their model can predict the dynamics of flow regimes "a" and "c" with satisfactory accuracy [15]. Two-equation models, such as the integral boundary layer model [16], the weighted residual model [17], and the integral energy model [18], were developed for when the flow rate is high to account for the inertial effect. Recent studies examined the influence of nozzle shape on the flow dynamics [19,20]. An interesting discovery is that the three different flow regimes, which were thought to be solely dependent on the flow rates, can be manipulated by adjusting the nozzle shape at a constant flow rate. In addition, the droplet spacing as well as the absolute-convective instability can be alternated by controlling the nozzle shape.

Most previous studies were operated in macroscale systems, and the surface tension σ is assumed to be either constant or correlated with other physical fields, e.g., the temperature field. It is well known that the dynamics of fluid flow is significantly dependent on the scales. For example, turbulence will not occur in micro- or nanoscale systems, which is widely seen in our daily lives, e.g., turbulent convection in the ocean and the atmosphere. The microscale, which quells the inertial effect, can bring about other extraordinary phenomena, which are unfamiliar in the macroscale of our daily lives [21]. For example, in biological systems, a lipid often has a hydrophobic head and one or several hydrophilic tails [22]. When dissolved in water, their heads are cumulated on the liquid surface, which reduces the surface tension and forms the interface elasticlike membrane. For instance, lipid drops coating stress fibers [23] and cotton fibers [24] play an important role in modulating the fibers' performance. The surface elasticity is small in the macrosituation, but it will be important in microcases. In addition, as the dimension goes down to the microregime, the surface tension was argued to be dependent on the radii of curvature [25]. The dependence of the surface tension of a liquid droplet on the droplet radius

*z.ding@hit.edu.cn

R was investigated by Tolman as early as 1949 [26]. He expanded the surface tension in power series of $1/R$, which correlates the surface tension and the spontaneous curvature $1/R$ at first order. Later, Helfrich made a more systematic expansion of the surface tension to second order [22]. Specifically, the new second-order terms were the bending rigidity or elasticity of a liquid surface. One term was proportional to $1/R^2$ and the other was proportional to the Gaussian curvature (saddle splay). Generalized curvature expansion of the surface tension σ was done by Sagis [27]:

$$\sigma = \sigma_0 - \widetilde{C}_b\widetilde{C}_0 H + \tfrac{1}{2}\widetilde{C}_b H^2 + \widetilde{C}_t K, \tag{1}$$

where σ_0 refers to the surface tension of a flat interface. It is therefore clear that the curvature elasticity is caused by the curvature-dependent surface tension. The second and third terms on the right-hand side of Eq. (1) are related to the mean curvature H—which is also called the spontaneous curvature, and it is characterized by parameters $\widetilde{C}_0$ and $\widetilde{C}_b$. The parameter $\widetilde{C}_b$ measures the bending rigidity of the interface, and $\widetilde{C}_0$ is usually defined as the spontaneous curvature parameter. The last term on the right-hand side of Eq. (1) is related to the Gaussian curvature K, which is characterized by the saddle-splay modulus $\widetilde{C}_t$. The coefficients $\widetilde{C}_0$, $\widetilde{C}_b$, and $\widetilde{C}_t$ are surface elasticity coefficients. These parameters are typically very small in macrocases, but they become important when the curvature is large, e.g., a microdroplet of radius $R \sim 1\ \mu$m. In the example of a thin liquid film coating a spider silk, we assume that the mean thickness of the film is of the same order as the spider silk radius ($\sim$0.5 μm). Hence, the mean radius of the liquid film is about 1 μm in the present work. The three coefficients of spontaneous curvature, bending rigidity, and saddle-splay modulus are $\widetilde{C}_0 \sim 1\ (\mu\text{m})^{-1}$, $\widetilde{C}_b \sim 3\times10^{-19}$ J, and $\widetilde{C}_t \sim 10^{-19}$ J at room temperature [28]. Patrascu and Balan [28] argued that the surface tension of a lipid-water solution is about $\sigma_0 \sim 1\ \mu$N/m or less. Thus, the curvature elasticity is important in this situation. For example, the spontaneous curvature term in (1) is about 0.5 μN/m and is comparable to σ_0. Dymond [29] gathered lipid spontaneous curvature data from the literature, where lipid monolayer spontaneous curvatures vary from 10^6 to 10^8 m^{-1}. Servuss *et al.* [30] measured the bending rigidity of a single egg lecithin bilayer, and showed $\widetilde{C}_b \in [2\times10^{-19}, 2.3\times10^{-19}$ J]. The saddle splay module can vary from 0 to 3×10^{-17} J [31,32]. In the present study, we assume that the saddle splay module is of order $O(10^{-20})$ J. For more information on the curvature elasticity of liquid surfaces, the reader can consult the review papers in Refs. [33,34].

A recent study examined the linear instability of a micro inviscid jet under the influence of curvature elasticity [28]. The results showed that the bending rigidity can either play a stabilizing role or a destabilizing role, depending on the spontaneous curvature (i.e., the jet radius), and the Gaussian curvature was found to suppress the Plateau-Rayleigh instability. A circular liquid film coating a solid core is similar to the jet flow in geometry but different in dynamics. The inner core plays a stabilizing role in the coating flow, which prevents the breakup of the film [35]. To the best of our knowledge, it is unclear how the curvature elasticity influences the Rayleigh-Plateau instability, and how the pattern formation in a circular liquid film flows on a microfiber. Another question that has yet to be answered is, does the viscosity matter? This paper aims to provide insights into these questions.

A synopsis of the paper is as follows. In Sec. II, the governing equations are stated. In this paper, since we are considering a thin film flowing down a microfiber, the fluid inertia is not important and there is no advantage of the two-equation models in this situation. Hence, Sec. III derives a single-equation model by extending the work of Craster and Matar [15]. Linear stability analysis is performed in Sec. IV, which is followed by a weakly nonlinear analysis in Sec. V. Section VI seeks steady traveling-wave solutions, which are brought about from Hopf bifurcation of the base state. Direct numerical simulations of the model equation are performed in Sec. VII to examine the nonlinear evolution and breakup of the interface. Finally, conclusions are presented in Sec. VIII.

II. MATHEMATICAL FORMULATION

We consider a Newtonian fluid with constant dynamic viscosity μ and density ρ, flowing down a vertical fiber as shown in Fig. 1. The radius of the cylindrical fiber is $r = a$. In the present study, we restrict ourselves to the axisymmetric problem, and the coordinates (r, z) are chosen. The system is governed by the continuity equation and the momentum equations:

$$u_r + \frac{u}{r} + w_z = 0, \tag{2}$$

$$\rho(u_t + uu_r + wu_z) = -p_r + \mu\left(u_{rr} + \frac{u_r}{r} - \frac{u}{r^2} + u_{zz}\right), \tag{3}$$

$$\rho(w_t + uw_r + ww_z) = \rho g - p_z + \mu\left(w_{rr} + \frac{w_r}{r} + w_{zz}\right), \tag{4}$$

where u and w denote the radial and axial velocity components, and g is the acceleration of gravity.

On the surface of the fiber $r = a$, we apply the nonslip and nonpenetration conditions:

$$u = w = 0. \tag{5}$$

At the liquid interface $R(z,t) = \alpha + h(z,t)$, the normal and tangential stresses are balanced by the surface tension:

$$\boldsymbol{T}\cdot\boldsymbol{n}\cdot\boldsymbol{t} = \nabla_s\sigma\cdot\boldsymbol{t}, \tag{6}$$

$$-p + \boldsymbol{T}\cdot\boldsymbol{n}\cdot\boldsymbol{n} + \frac{A'}{6\pi(R-\alpha)^3} = 2\sigma H,$$

$$2H = \frac{R_{zz}}{\left(1+R_z^2\right)^{3/2}} - \frac{1}{R\left(1+R_z^2\right)^{1/2}}, \tag{7}$$

where $h(z,t)$ is the film thickness, $\boldsymbol{T} = \mu[\nabla\boldsymbol{u} + (\nabla\boldsymbol{u})^T]$ is Newtonian viscous stress, $\boldsymbol{n} = \frac{(\boldsymbol{e}_r, -R_z\boldsymbol{e}_z)}{\sqrt{1+R_z^2}}$ is the surface normal, $\boldsymbol{t} = \frac{(R_z\boldsymbol{e}_r, \boldsymbol{e}_z)}{\sqrt{1+R_z^2}}$ is the surface tangent, and $\nabla_s = \nabla - \boldsymbol{n}(\boldsymbol{n}\cdot\nabla)$ is the surface gradient operator. A' is the Hamaker constant, and its value represents the magnitude of the Van der Waals forces. The surface tension is assumed to be dependent on the curvature as shown in (1), and the Gaussian curvature K is defined as

$$K = \frac{-R_{zz}}{R\left(1+R_z^2\right)^2}. \tag{8}$$

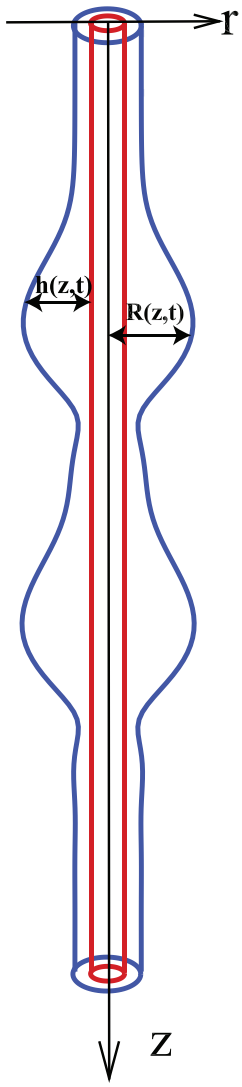

FIG. 1. Sketch of the system: a liquid film flowing down a vertical fiber.

We note that the spontaneous curvature and the Gaussian curvature are important only for a circular or spherical interface, which are negligible in liquid films flowing down a planar surface. In the present study the Van der Waals forces are considered, which are characterized by the Hamaker number A' [36]. In the study by Ji *et al.* [7], the Van der Waals forces were treated as repelling forces ($A' < 0$), which was found to prevent the breakup of the liquid interface. Ding *et al.* [35] showed that Van der Waals forces play an adverse role when $A' > 0$, which accounts for the finite-time breakup of the liquid film. But it is still unclear whether the surface elasticity can prevent the breakup of the liquid film when $A' > 0$, which will be examined later in Sec. V.

Finally, the system is closed by the kinematic condition of the interface,

$$R_t + wR_z = u. \tag{9}$$

III. SCALING AND ASYMPTOTIC MODEL

A. Scalings

We choose the mean radius of the liquid film $\mathcal{R}$ and the capillary length $\mathcal{L} = \sigma_0/(\rho g \mathcal{R})$ as the radial and axial length scales, $\rho g \mathcal{L}$, and $\mathcal{W} = \rho \mathcal{R}^2 g/\mu$ as the pressure and velocity scales. Hence, the dimensionless form of the governing equations reads

$$u_r + \frac{u}{r} + w_z = 0, \tag{10}$$

$$\epsilon^4 La(u_t + uu_r + wu_z) = -p_r + \epsilon^2\left(u_{rr} + \frac{u_r}{r} - \frac{u}{r^2} + \epsilon^2 u_{zz}\right), \tag{11}$$

$$\epsilon^2 La(w_t + uw_r + ww_z) = 1 - p_z + \left(w_{rr} + \frac{w_r}{r} + \epsilon^2 w_{zz}\right). \tag{12}$$

Since the present work considers a thin liquid layer coating a microfiber ($\mathcal{R} \sim 10^{-6}$ m) and a low surface tension situation ($\sigma_0 < 10^{-6}$ N/m [28]), the Laplace number $\mathrm{La} = \sigma_0 \rho \mathcal{R}/\mu^2$, which was also defined as the Reynolds number by Craster and Matar [15], is very small, $\mathrm{La} \ll 1$, and therefore the inertial terms can be safely neglected. The parameter $\epsilon = \mathcal{R}/\mathcal{L} = \rho g \mathcal{R}^2/\sigma_0$ is the Bond number, and $\epsilon \sim 10^{-1}$ in the present study.

At the interface $r = R(z,t)$, the dimensionless normal and tangent stress balance conditions are

$$\begin{aligned} p - \frac{\epsilon A_H}{La(R-\alpha)^3} - \frac{2\epsilon^2}{1+\epsilon^2 R_z^2}\left[u_r - \left(w_r + \epsilon^2 u_z\right)R_z + \epsilon^2 w_z R_z^2\right] \\ = \frac{1}{R} - \epsilon^2 R_{zz} + \frac{\epsilon C_b C_0}{2}\left(\frac{1}{R^2} - \frac{2\epsilon^2 R_{zz}}{R}\right) \\ - C_t \frac{\epsilon^3 R_{zz}}{R^2} - \frac{\epsilon C_b}{8}\left(\frac{3\epsilon^2 R_{zz}}{R^2} - \frac{1}{R^3}\right) + O(\epsilon^4), \end{aligned} \tag{13}$$

$$\begin{aligned} w_r = -\frac{C_b C_0}{2}\left(\epsilon^3 R_{zzz} + \frac{\epsilon R_z}{R^2}\right) - C_t \frac{\epsilon^3 R_{zzz}}{R} \\ - \frac{C_b}{4}\left(\frac{\epsilon^3 R_{zzz}}{R} + \frac{\epsilon R_z}{R^3}\right), \end{aligned} \tag{14}$$

where higher-order terms of $O(\epsilon^4)$ are neglected, and $C_0 = \widetilde{C}_0 \mathcal{R} \sim O(1)$ is defined as the dimensionless spontaneous curvature parameter, $C_b = \frac{\widetilde{C}_b}{\sigma_0 \mathcal{R}^2} \sim O(1)$ is defined as the dimensionless bending rigidity parameter, and $C_t = \frac{\widetilde{C}_t}{\sigma_0 \mathcal{R}^2} \sim O(10^{-1})$ is the dimensionless saddle splay parameter. $A_H = \frac{A'\sigma_0}{6\pi g \mathcal{R}^3 \mu^2} \sim O(10^{-5})$ is defined as the dimensionless Hamaker number. Hence, following Ding *et al.* [35], a composite Hamaker number $A = A_H/\mathrm{La}$ is of order $O(10^{-1})$ as $\mathrm{La} \sim O(10^{-4})$.

The dimensionless boundary conditions on the fiber surface $r = \alpha$ ($\alpha = a/\mathcal{R}$ being the dimensionless fiber radius) and the kinematic condition of the interface at $r = R(z,t)$ remain the same as their dimensional versions.

B. Long-wave model

The leading-order dynamics of the system is governed by

$$u_r + \frac{u}{r} + w_z = 0, \tag{15}$$

$$p_r = 0, \tag{16}$$

$$1 - p_z + w_{rr} + \frac{w_r}{r} = 0. \tag{17}$$

$$w|_{r=\alpha} = 0,\ w_r|_{r=\alpha+h(z,t)} = \mathcal{M}, \tag{18}$$

$$p = \frac{\epsilon A}{(R-\alpha)^3} + \frac{1}{R} - \epsilon^2 R_{zz} + \frac{\epsilon C_b C_0}{2}\left(\frac{1}{R^2} - \frac{2\epsilon^2 R_{zz}}{R}\right) - C_t\frac{\epsilon^3 R_{zz}}{R^2} - \frac{\epsilon C_b}{8}\left(\frac{3\epsilon^2 R_{zz}}{R^2} - \frac{1}{R^3}\right), \tag{19}$$

where $\mathcal{M} = w_r|_{r=\alpha+h(z,t)} = -\frac{C_b C_0}{2}(\epsilon^3 R_{zzz} + \frac{\epsilon R_z}{R^2}) - C_t\frac{\epsilon^3 R_{zzz}}{R} - \frac{C_b}{4}(\frac{\epsilon^3 R_{zzz}}{R} + \frac{\epsilon R_z}{R^3})$. Inclusion of the higher-order terms up to $O(\epsilon^3)$ in (18) and (19) is ad hoc, which is under the consideration of capturing the effects of curvature elasticity but not making the model very complicated. For a liquid film flowing down a fiber (radius about 1 mm), Craster and Matar showed that the second-order term $\epsilon^2 R_{zz}$ should be included in the model since it is essential to yield the correct cutoff wave number as reflected by the linear stability analysis [15]. In the present study, linear stability analysis also suggests that inclusion of these higher-order terms can yield accurate predictions of the long-wave dynamics in the considered range of C_b, C_0, and C_t (see Fig. 2).

Solving Eq. (17) subjected to boundary conditions (18) gives the solution of w,

$$w = \left[\mathcal{M}R - \frac{R^2(p_z-1)}{2}\right]\ln(r/\alpha) + \frac{r^2-\alpha^2}{4}(p_z-1). \tag{20}$$

Substituting the velocity w into the kinematic equation, we obtain the evolution equation of the film radius $R(z,t)$,

$$R_t + R^{-1}q_z = 0, \tag{21}$$

with

$$q = \left[-\frac{p_z-1}{4}R^2 + \frac{\mathcal{M}R}{2}\right]\left[R^2\ln\left(\frac{R}{\alpha}\right) - \frac{R^2-\alpha^2}{2}\right] + \frac{p_z-1}{4}\frac{(R^2-\alpha^2)^2}{4}.$$

The pressure gradient p_z can be calculated from Eq. (19). Equation (22) is identical to Craster and Matar's equation [15] when curvature elasticity and Van der Waals attractions are turned off.

IV. LINEAR STABILITY ANALYSIS

Equation (21) has the following trivial solution:

$$R = 1, \quad q = \tfrac{1}{16}[-4\ln\alpha - (1-\alpha^2)(3-\alpha^2)]. \tag{22}$$

Linear stability of the trivial solution $R = 1$ is investigated by perturbing it with infinitesimal disturbance. Using the normal mode analysis, i.e., $R = 1 + \hat{R}\exp(ikz + \lambda t)$ ($\hat{R} \ll 1$, k is the wave number, and $\lambda = \lambda_r + i\lambda_i$ is the complex growth rate), and after linearizing, we obtain the following dispersion relation:

$$\lambda_r = \left(-\frac{1}{4}\ln\alpha - \frac{1-\alpha^2}{8} - \frac{(1-\alpha^2)^2}{16}\right)\left(\frac{3\epsilon^3 A k^2}{(1-\alpha)^4} + \epsilon^2 k^2 - \epsilon^4 k^4\right) + \epsilon^5 C_t k^4\left(-\frac{1}{4}\ln\alpha - \frac{1-\alpha^2}{8} + \frac{(1-\alpha^2)^2}{16}\right) + \epsilon C_b(\epsilon^2 k^2 - \epsilon^4 k^4)\left(\frac{1}{32}\ln\alpha + \frac{1-\alpha^2}{64} - \frac{(1-\alpha^2)^2}{16} - \frac{(1-\alpha^2)^2}{16}C_0 - \frac{3(1-\alpha^2)^2}{128}\right), \tag{23}$$

$$\lambda_i = \frac{k}{2}(2\ln\alpha + 1 - \alpha^2). \tag{24}$$

Introducing $\omega = \epsilon\lambda$ and $\kappa = \epsilon k$, we rewrite the dispersive relation as

$$\omega_r = \left(-\ln\alpha - \frac{1-\alpha^2}{2}\right)\mathscr{A} - \frac{(1-\alpha^2)^2}{16}\mathscr{B}, \tag{25}$$

$$\omega_i = \frac{\kappa}{2}(2\ln\alpha + 1 - \alpha^2), \tag{26}$$

in which

$$\mathscr{A} = \frac{1}{4}\left[\frac{3A\kappa^2}{(1-\alpha)^4} + \left(\Sigma_0 - \frac{C_b}{8}\right)(\kappa^2 - \kappa^4) + C_t\kappa^4\right],$$

$$\mathscr{B} = \frac{3A\kappa^2}{(1-\alpha)^4} + \left(\Sigma_0 + C_b C_0 + \frac{3C_b}{8}\right)(\kappa^2 - \kappa^4) - C_t\kappa^4,$$

and $\Sigma_0 = \epsilon^{-1}$. A critical wave number κ_c, corresponding to $\omega_r = 0$, is defined as follows:

$$\kappa_c = \sqrt{\frac{\left(\frac{3A}{4(1-\alpha)^4} + \frac{\Sigma_0}{4} - \frac{C_b}{32}\right)\left(-\ln\alpha - \frac{1-\alpha^2}{2}\right) - \frac{(1-\alpha^2)^2}{16}\left[\frac{3A}{(1-\alpha)^4} + \Sigma_0 + C_b C_0 + \frac{3C_b}{8}\right]}{\left(\frac{\Sigma_0}{4} - \frac{C_t}{4} - \frac{C_b}{32}\right)\left(-\ln\alpha - \frac{1-\alpha^2}{2}\right) - \frac{(1-\alpha^2)^2}{16}\left(\Sigma_0 + C_b C_0 + \frac{3C_b}{8}\right)}}. \tag{27}$$

When curvature elasticity and van der Waals forces are inactive, $\kappa_c = 1$ is obtained, which corresponds to the classical result for the Plateau-Rayleigh instability. For $\kappa < \kappa_c$ the interface is linearly unstable, and for $\kappa > \kappa_c$ the interface is linearly stable.

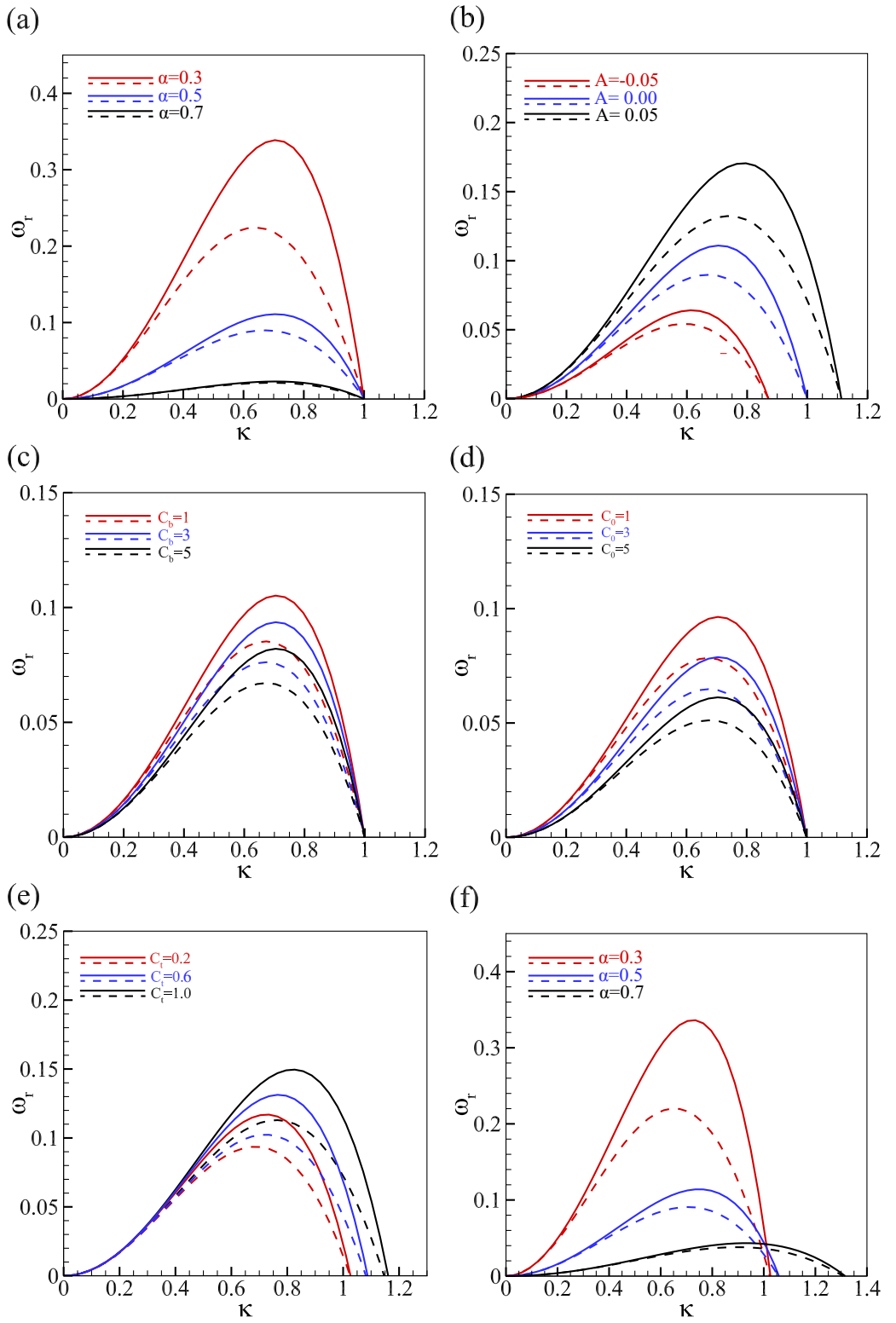

FIG. 2. Comparisons between the linear stability analysis of the Navier-Stokes equations (dashed lines) and the long-wave model (solid lines). The Bond number is fixed at $\epsilon = 0.1$. (a) $C_b = 0$, $C_0 = 0$, $C_t = 0$, $A = 0$; (b) $C_b = 0$, $C_0 = 0$, $C_t = 0$, $\alpha = 0.5$; (c) $C_0 = 0$, $C_t = 0$, $A = 0$, $\alpha = 0.5$; (d) $C_b = 1$, $C_t = 0$, $A = 0$, $\alpha = 0.5$; (e) $C_b = 0$, $C_0 = 0$, $A = 0$; and (f) $C_b = 1$, $C_0 = 1$, $C_t = 0.2$, $A = 0.01$.

When the curvature elasticity and Van der Waals attractions are turned off, our results are identical to those of Craster and Matar [15], and the flow is more stable when the fiber is thicker, as demonstrated in Fig. 2(a). In Fig. 2(b), we vary the composite Hamaker number and find that Van der Waals attractions (positive A) enhance the Plateau-Rayleigh mechanism, while the repulsions (negative A) weaken the Plateau-Rayleigh mechanism. Figure 2(c) illustrates the

influence of the surface bending rigidity on the linear stability, demonstrating that it plays a stabilizing role in the system. Indeed, Eq. (23) indicates that surface bending rigidity and spontaneous curvature always reduce the growth rate [see also Fig. 2(d)]. If the surface bending rigidity is absent, the spontaneous curvature will be muted. Clearly, our results are different from the study by Patrascu and Balan [28], who showed that the bending rigidity either plays a stabilizing role or a destabilizing role, which depends on the radius of the jet. A scrutiny of their study indicates that the different conclusion by Patrascu and Balan [28] is caused by an error expansion in the spontaneous curvature. The Gaussian curvature plays an adverse role, which promotes the instability as seen in Fig. 2(e). Such an observation is also completely different from the study by Patrascu and Balan [28], who reported that Gaussian curvature plays a stabilizing role in the inviscid jet. To account for the instability mechanism of Gaussian curvature, we examine the normal stress balance condition in Eq. (19) and the tangential stress balance condition in Eq. (18). In the normal stress balance condition, we have known that the streamwise curvature term $-\epsilon^2 R_{zz}$ plays a stabilizing role. In analogy with the streamwise curvature, the Gaussian curvature should be a stabilizing role in the normal stress balance condition. To understand its effect in the tangential stress balance condition, we assume that the interface is perturbed by a small disturbance, $\delta \sin(kz)$ ($\delta \ll 1$), such that the term associated with the Gaussian curvature is $C_t \delta k^3 \cos(kz)$. Hence, the surface tension contributed by the Gaussian curvature is driving the liquid out from the troughs into the crests, thus enhancing the deformation of the interface and instability. Thanks to the viscosity, the tangential component is double the normal component, and the Gaussian curvature becomes a destabilizing effect in the viscous flow. For an inviscid flow on the fiber, the Gaussian curvature should be a stabilizing effect, as is that in the inviscid jet flow. It is interesting that the cutoff wave number predicted by our long-wave model agrees well with the result by linearized Navier-Stokes equations (LNS) in Figs. 2(a)–2(d). The agreement, however, deteriorates as the Gaussian curvature becomes large, as seen in Fig. 2(e). The linear stability analysis showed that only the spontaneous curvature parameter C_0 is dependent on the bending rigidity parameter C_b. The Gaussian curvature effect, Van der Waals attractions, and the bending rigidity are independent effects. So, a net effect will be a linear superposition of these effects. Figure 2(f) shows that comparison between the long-wave model and the Navier-Stokes equations wherein both the curvature elasticity and Van der Waals attractions are turned on. The results demonstrate that our model is reasonable in the long-wave regime ($\kappa \ll 1$), and the model becomes more accurate for thinner films when the Bond number is constant.

V. WEAKLY NONLINEAR STABILITY

After exploring the linear stability, this section aims to understand the curvature elasticity on the weakly nonlinear stability of the system. Instead of using the liquid radius R as the variable, we use a new variable, $S = R^2$, which is proportional to the cross-sectional area, to investigate the weakly nonlinear stability. This is so because the fluid volume is conserved during the nonlinear evolution when the interface is perturbed by a wavelike disturbance [14]. In addition, in all of the previous literature, the fully nonlinear solution to the evolution equation of the interface was sought by fixing the liquid volume, which will also be enforced in Sec. VI. Hence, to compare the analytical results of the weakly nonlinear analysis with the fully nonlinear solution, we must also fix the fluid volume in the weakly nonlinear analysis. Therefore, we restate Eq. (21) as

$$S_t + \mathcal{A}(S)S_z + \mathcal{B}(S)S_{zz} + C(S)S_{zzzz} + \mathcal{D}(S)S_z^2 + \mathcal{E}(S)S_z S_{zzz} = 0, \tag{28}$$

where

$$\mathcal{A}(S) = 2S^{\frac{1}{2}}\left(S\ln\frac{S^{\frac{1}{2}}}{\alpha} - \frac{S-\alpha^2}{2}\right),$$

$$\mathcal{B}(S) = \left(\frac{3\epsilon AS}{2(S^{\frac{1}{2}}-\alpha)^4} + \frac{\epsilon\Sigma}{2} - \frac{\epsilon C_b}{16S}\right)\left(S\ln\frac{S^{\frac{1}{2}}}{\alpha} - \frac{S-\alpha^2}{2}\right) - \frac{\epsilon(S-\alpha^2)^2}{8}\left(\frac{3A}{(S^{\frac{1}{2}}-\alpha)^4} + \frac{\Sigma}{S} + \frac{C_bC_0}{S^{\frac{3}{2}}} + \frac{3C_b}{8S^2}\right),$$

$$C(S) = \left(\frac{\epsilon^3 S\Sigma}{2} - \frac{\epsilon^3 C_t}{2} - \frac{\epsilon^3 C_b}{16}\right)\left(S\ln\frac{S^{\frac{1}{2}}}{\alpha} - \frac{S-\alpha^2}{2}\right) - \frac{\epsilon^3(S-\alpha^2)^2}{8}\left(\Sigma + \frac{C_bC_0}{S^{\frac{1}{2}}} + \frac{C_t}{S} + \frac{3C_b}{8S}\right),$$

$$\mathcal{D}(S) = \left[\frac{(S-\alpha^2)^2}{8} - \frac{S}{2}\left(S\ln\frac{S^{\frac{1}{2}}}{\alpha} - \frac{S-\alpha^2}{2}\right)\right]\left(\frac{12\epsilon A}{(S^{\frac{1}{2}}-\alpha)^5} + \frac{2}{S^{\frac{3}{2}}} + \frac{3\epsilon C_bC_0}{S^2} + \frac{3\epsilon C_b}{2S^{\frac{5}{2}}}\right)$$
$$+ \left(S\ln\frac{S^{\frac{1}{2}}}{\alpha} - \frac{S-\alpha^2}{2}\right)\left(\frac{6\epsilon AS^{\frac{1}{2}}}{(S^{\frac{1}{2}}-\alpha)^4} + \frac{2}{S^{\frac{1}{2}}} + \frac{3\epsilon C_bC_0}{S} + \frac{3\epsilon C_b}{2S^{\frac{3}{2}}}\right), + \left(3S\ln\frac{S^{\frac{1}{2}}}{\alpha} - \frac{S-\alpha^2}{2}\right)\left(-\frac{\epsilon C_bC_0}{2S} - \frac{\epsilon C_b}{4S^{\frac{3}{2}}}\right),$$

$$\mathcal{E}(S) = \left(S\ln\frac{S^{\frac{1}{2}}}{\alpha} - \frac{S-\alpha^2}{2}\right)\left(2\epsilon^2 S^{\frac{1}{2}} + 2\epsilon^3 C_bC_0 + \frac{3\epsilon^3 C_t}{S^{\frac{1}{2}}} + \frac{\epsilon^3 C_b}{S^{\frac{1}{2}}}\right) + \left(3S\ln\frac{S^{\frac{1}{2}}}{\alpha} - \frac{S-\alpha^2}{2}\right)\left(-\frac{\epsilon^3 C_bC_0}{2} - \frac{\epsilon^3 C_t}{S^{\frac{1}{2}}} - \frac{\epsilon^3 C_b}{4S^{\frac{1}{2}}}\right)$$

When the interface is perturbed by small-finite amplitude disturbances, by setting $S = 1 + \eta(t, z)$ ($\|\eta\| \ll 1$) and after retaining the terms up to $O(\eta^3)$, Eq. (28) is reduced as

$$\begin{aligned}
&\eta_t + \bar{\mathcal{A}}\eta_z + \bar{\mathcal{B}}\eta_{zz} + \bar{\mathcal{C}}\eta_{zzzz} + \bar{\mathcal{D}}\eta_z^2 + \bar{\mathcal{E}}\eta_z\eta_{zzz} \\
&+ \left(\bar{\mathcal{A}}'\eta + \frac{\bar{\mathcal{A}}''}{2}\eta^2\right)\eta_z + \left(\bar{\mathcal{B}}'\eta + \frac{\bar{\mathcal{B}}''}{2}\eta^2\right)\eta_{zz}, \\
&+ \left(\bar{\mathcal{C}}'\eta + \frac{\bar{\mathcal{C}}''}{2}\eta^2\right)\eta_{zzzz} + \left(\bar{\mathcal{D}}'\eta + \frac{\bar{\mathcal{D}}''}{2}\eta^2\right)\eta_z^2 \\
&+ \left(\bar{\mathcal{E}}'\eta + \frac{\bar{\mathcal{E}}''}{2}\eta^2\right)\eta_z\eta_{zzz} + O(\eta^4) = 0, \qquad (29)
\end{aligned}$$

in which the primes stand for derivatives with respect to z, and the overbar indicates that the polynomial is evaluated at the unperturbed state, i.e., $S = 1$. To account for the nonlinear effect, we invoke the multiscale expansion technique here [37]:

$$\frac{\partial}{\partial t} \to \frac{\partial}{\partial t} + \zeta\frac{\partial}{\partial t_1} + \zeta^2\frac{\partial}{\partial t_2}, \qquad (30)$$

$$\frac{\partial}{\partial z} \to \frac{\partial}{\partial z} + \zeta\frac{\partial}{\partial z_1}, \qquad (31)$$

$$\eta(z, z_1, t, t_1, t_2; \zeta) = \zeta\eta_1 + \zeta^2\eta_2 + \zeta^3\eta_3, \qquad (32)$$

where ζ is a small perturbation parameter, and $\zeta = k - k_c$ in the present work. Therefore, Eq. (29) is expanded to

$$(L_0 + \zeta L_1 + \zeta^2 L_2)(\zeta\eta_1 + \zeta^2\eta_2 + \zeta^3\eta_3) = -\zeta^2 N_2 - \zeta^3 N_3, \qquad (33)$$

where

$$L_0 = \frac{\partial}{\partial t} + \bar{\mathcal{A}}\frac{\partial}{\partial z} + \bar{\mathcal{B}}\frac{\partial^2}{\partial z^2} + \bar{\mathcal{C}}\frac{\partial^4}{\partial z^4}, \quad L_1 = \frac{\partial}{\partial t_1} + \bar{\mathcal{A}}\frac{\partial}{\partial z_1} + 2\bar{\mathcal{B}}\frac{\partial^2}{\partial z\partial z_1} + 4\bar{\mathcal{C}}\frac{\partial^4}{\partial z^3\partial z_1},$$

$$L_2 = \frac{\partial}{\partial t_2} + \bar{\mathcal{B}}\frac{\partial^2}{\partial z_1^2} + 6\bar{\mathcal{C}}\frac{\partial^4}{\partial z^2\partial z_1^2}, \quad N_2 = \bar{\mathcal{A}}'\eta_1\eta_{1,z} + \bar{\mathcal{B}}'\eta_1\eta_{1,zz} + \bar{\mathcal{C}}'\eta_1\eta_{1,zzzz} + \bar{\mathcal{D}}\eta_{1,z}^2 + \bar{\mathcal{E}}\eta_{1,z}\eta_{1,zzz},$$

$$\begin{aligned}
N_3 = {} & \bar{\mathcal{A}}'(\eta_1\eta_{2,z} + \eta_{1,z}\eta_2 + \eta_1\eta_{1,z_1}) + \bar{\mathcal{B}}'(\eta_1\eta_{2,zz} + 2\eta_1\eta_{1,zz_1} + \eta_{1,zz}\eta_2) \\
& + \bar{\mathcal{C}}'(\eta_1\eta_{2,zzzz} + 4\eta_1\eta_{1,zzzz_1} + \eta_{1,zzzz}\eta_2) + \bar{\mathcal{D}}(2\eta_{1,z}\eta_{2,z} + 2\eta_{1,z}\eta_{1,z_1}) \\
& + \bar{\mathcal{E}}(\eta_{1,z}\eta_{2,zzz} + 3\eta_{1,z}\eta_{1,zzz_1} + \eta_{1,zzz}\eta_{2,z} + \eta_{1,zzz}\eta_{1,z_1}) + \tfrac{1}{2}\bar{\mathcal{A}}''\eta_1^2\eta_{1,z} + \tfrac{1}{2}\bar{\mathcal{B}}''\eta_1^2\eta_{1,zz} \\
& + \tfrac{1}{2}\bar{\mathcal{C}}''\eta_1^2\eta_{1,zzzz} + \bar{\mathcal{D}}'\eta_1\eta_{1,z}^2 + \bar{\mathcal{E}}'\eta_1\eta_{1,z}\eta_{1,zzz}.
\end{aligned}$$

The leading-order $O(\zeta)$ problem solves the following linear eigenvalue equation:

$$L_0\eta_1 = 0, \qquad (34)$$

which admits the harmonic-wave solution

$$\eta_1 = a(t_1, t_2; z_1)\exp[i(kz + \lambda_i t)] + \text{c.c.} \qquad (35)$$

Here $\lambda_i = -\bar{\mathcal{A}}k$, $\lambda_r = \bar{\mathcal{B}}k^2 - \bar{\mathcal{C}}k^4 = O(\epsilon^2)$, and $k = \sqrt{\bar{\mathcal{B}}/\bar{\mathcal{C}}}$. Because λ_r is small, the slowly time-varying term is absorbed by the amplitude a. At order $O(\zeta^2)$, we solve

$$L_0\eta_2 = -L_1\eta_1 - N_2. \qquad (36)$$

By inserting η_1 into Eq. (36), we have

$$\begin{aligned}
L_0\eta_2 = {} & -\left[\frac{\partial a}{\partial t_1} + (\bar{\mathcal{A}} + 2ik\bar{\mathcal{B}} - 4ik^3\bar{\mathcal{C}})\frac{\partial a}{\partial z_1}\right]e^{i(kz+\lambda_i t)} \\
& - (i\bar{\mathcal{A}}'k + \bar{\mathcal{B}}'k^2 - \bar{\mathcal{C}}'k^4 + \bar{\mathcal{D}}k^2 - \bar{\mathcal{E}}k^4) \\
& \times a^2 e^{2i(kz+\lambda_i t)} + \text{c.c.} \qquad (37)
\end{aligned}$$

The solvability condition of the $O(\epsilon^2)$ problem requires that the forcing term on the right-hand side of Eq. (37) is orthogonal to the null-space of L_0^+ (the adjoint operator of L_0). Hence, we have

$$\frac{\partial a}{\partial t_1} + (\bar{\mathcal{A}} + 2ik\bar{\mathcal{B}} - 4ik^3\bar{\mathcal{C}})\frac{\partial a}{\partial z_1} = 0, \qquad (38)$$

and the solution of a is followed by

$$a(t_1, t_2; z_1) = a(t_2)e^{ik[z_1 - (\bar{\mathcal{A}} + 2ik\bar{\mathcal{B}} - 4ik^3\bar{\mathcal{C}})t_1]}. \qquad (39)$$

Hence, Eq. (37) admits the following solution:

$$\eta_2 = e_0 a^2\exp[2i(kz + \lambda_i t)] + \text{c.c.} \qquad (40)$$

Here, $e_0 = e_r + ie_i = \frac{\bar{\mathcal{B}}' - \bar{\mathcal{C}}'k^2 + \bar{\mathcal{D}} - \bar{\mathcal{E}}k^2}{16\bar{\mathcal{C}}k^2 - 4\bar{\mathcal{B}}} + i\frac{-\bar{\mathcal{A}}'}{16\bar{\mathcal{C}}k^3 - 4\bar{\mathcal{B}}k}$.

Furthermore, we proceed to the third-order problem:

$$L_0\eta_3 + \zeta^{-2}L_0\eta_1 + L_1\eta_2 + L_2\eta_1 = -N_3. \qquad (41)$$

Similarly, the solvability condition of Eq. (41) gives the following Landau-type equation:

$$\frac{\partial a}{\partial t_2} + (\bar{\mathcal{B}} - 6\bar{\mathcal{C}}k^2)\frac{\partial^2 a}{\partial z_1^2} - \zeta^{-2}\lambda_r a + (J_2 + iJ_4)a^2 a^* = 0, \qquad (42)$$

where

$$\begin{aligned}
J_2 = {} & (-5\bar{\mathcal{B}}'k^2 + 17\bar{\mathcal{C}}'k^4 + 4\bar{\mathcal{D}}k^2 - 10\bar{\mathcal{E}}k^4)e_r - \bar{\mathcal{A}}'ke_i \\
& + \left(-\tfrac{3}{2}\bar{\mathcal{B}}''k^2 + \tfrac{3}{2}\bar{\mathcal{C}}''k^4 + \bar{\mathcal{D}}'k^2 - \bar{\mathcal{E}}'k^4\right), \\
J_4 = {} & (-5\bar{\mathcal{B}}'k^2 + 17\bar{\mathcal{C}}'k^4 + 4\bar{\mathcal{D}}k^2 - 10\bar{\mathcal{E}}k^4)e_i + \bar{\mathcal{A}}'ke_r \\
& + \tfrac{1}{2}\bar{\mathcal{A}}''k. \qquad (43)
\end{aligned}$$

For a filtered wave, which has no spatial modulation, the diffusion term in Eq. (42) can be dropped and the amplitude a obeys the following simple form:

$$a = a_0\exp[-ib(t_2)t_2] \qquad (44)$$

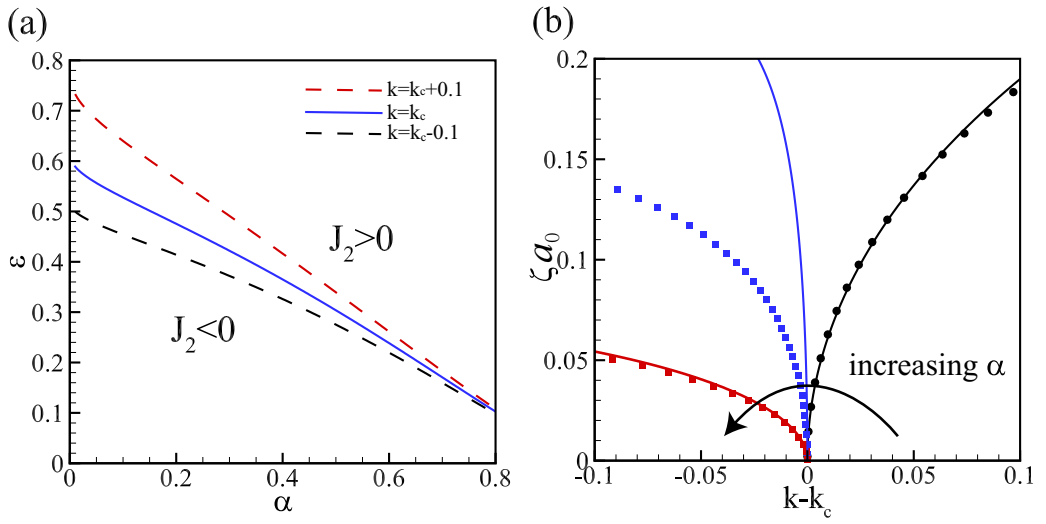

FIG. 3. (a) The $J_2 = 0$ curve with different k in the α-ϵ plane. (b) The perturbation amplitude ζa vs $k - k_c$ at different α. The other parameters are $A = 0$, $C_b = 0$, $C_0 = 0$, $C_t = 0$, $\epsilon = 0.25$, and $k = k_c$. Solid lines are results from weakly nonlinear analysis, dots are results from traveling-wave solutions. The value of α is marked by different colors: red, blue, and black are for $\alpha = 0.20$, 0.59, and 0.75, respectively.

and

$$\frac{\partial a_0}{\partial t_2} = \left(\zeta^{-2}\lambda_r - J_2 a_0^2\right)a_0, \tag{45}$$

$$\frac{\partial (b(t_2)t_2)}{\partial t_2} = J_4 a_0^2. \tag{46}$$

The amplitude for a saturated wave is given by

$$\zeta a_0 = \sqrt{\frac{\lambda_r}{J_2}}. \tag{47}$$

Estimating the critical amplitude is important for choosing a convergent initial guess for exact invariant solutions to the nonlinear evolution equation (21). If the amplitude of the initial guess is not well chosen, the nonlinear exact invariant solution (e.g., the traveling-wave solution or the periodic orbit) either diverges or converges to the unperturbed solution. The sign of J_2 is crucial to determine the instability characteristics of the flow. To illustrate this, we plot $J_2 = 0$ in the α-ϵ plane by fixing $k = k_c$, $k_c \pm 0.1$ as seen in Fig. 3(a). We have known that the flow is linearly stable for $k = k_c + 0.1$ and linearly unstable for $k = k_c - 0.1$. Hence, in the α-ϵ plane, the curve for $k = k_c$ marks the boundary for the supercritical ($\lambda_r > 0, J_2 > 0$) and subcritical ($\lambda_r < 0, J_2 < 0$) instabilities, i.e., below the curve the instability is subcritical and the above regime is supercritical. To further illustrate the supercritical and subcritical instabilities, we deactivate the van der Waals attractions and the curvature elasticity, and we plot the amplitude of saturated waves against the distance away from the linear stability $k = k_c$, which is shown in Fig. 3(b). It is clear that the fiber radius plays an important role in determining the stability type: by increasing the fiber radius (or reducing the film thickness), the instability transits from subcritical to supercritical. And our results agree with the bifurcation analysis of the fully nonlinear model excellently (the nonlinear traveling-wave solutions are sought in Sec. VI). But the agreement deteriorates near the transitional boundary, i.e., the critical fiber radius $\alpha_c \approx 0.59$, which is due to the neglected higher-order terms in the weakly nonlinear analysis.

Figure 4(a) demonstrates that the Van der Waals attractions promote subcritical instability when the fiber is thin, and supercritical instability when the fiber is thick (roughly $\alpha > 0.6$). The effects of the bending rigidity and spontaneous curvature on the weakly nonlinear stability are more complicated. As seen in Figs. 4(b) and 4(c), as C_b and C_0 increases, the contour line develops into a sandwich structure: $J_2 > 0$ in the middle region and $J_2 < 0$ in the side regions. This implicates that the bending rigidity and spontaneous curvature are playing dual roles in determining the subcritical or supercritical stability. For instance, in Craster and Matar [15], their flow regime "c" (wherein a large droplet coexists with several tiny small beads) is subcritically unstable. When the bending rigidity $C_b \gtrsim 4.6$ or the spontaneous curvature parameter $C_0 \gtrsim 3.1$, the subcritical instability is completely suppressed and the instability transits to supercritical (see more illustrative plots in Fig. 5). The Gaussian curvature, however, plays an adverse role in the Van der Waals attractions, which suppresses the subcritical instability when the fiber is thin, and the supercritical instability when the fiber is thick, as demonstrated in Fig. 4(d).

VI. PRIMARY BIFURCATION AND TRAVELING-WAVE SOLUTION

To explore the influence of various parameters on nonlinear solutions, we seek the coherent nonlinear traveling-wave solutions, which were widely used to understand the formation of organized droplets in previous studies [14,15]. Introducing the following traveling-wave transformation:

$$\xi = z - ct, \tag{48}$$

and setting $R(z,t) = R(\xi)$, the evolution equation (21) transforms into

$$-cRR_\xi + q_\xi = 0, \tag{49}$$

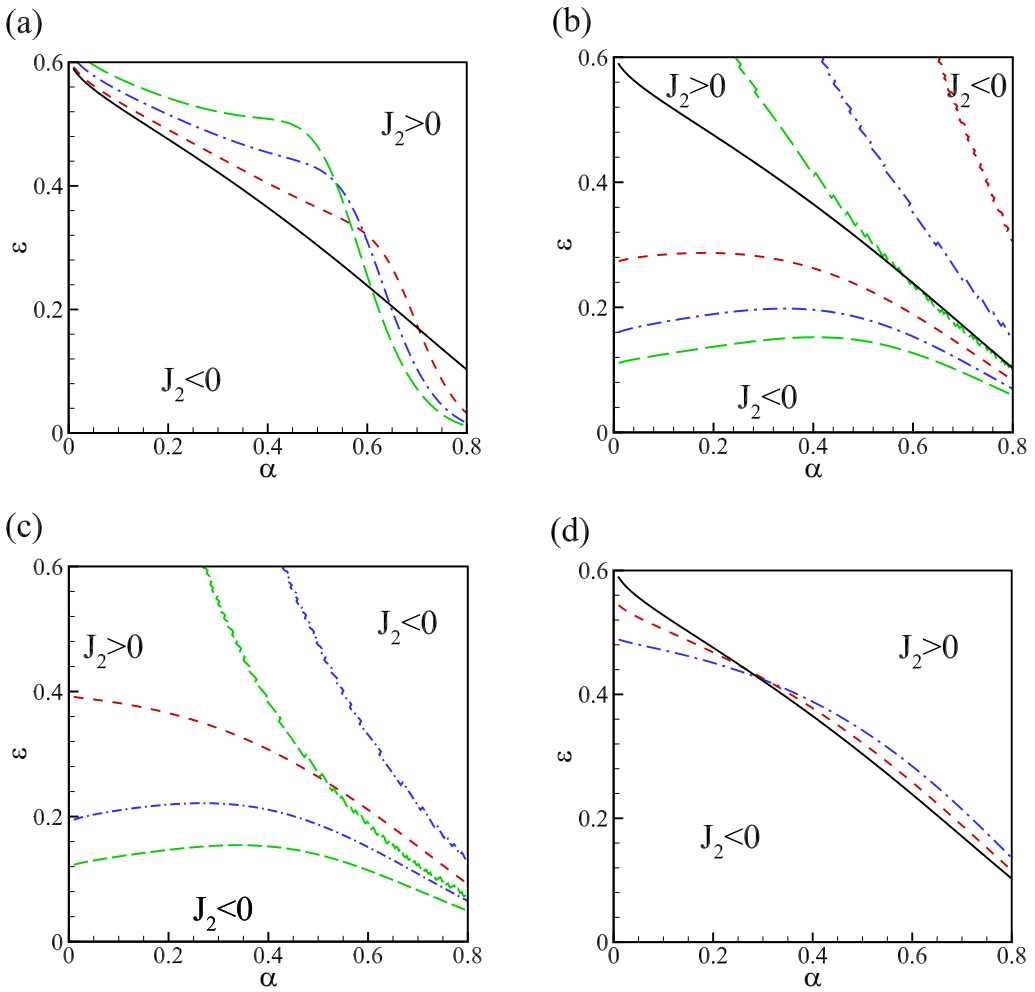

FIG. 4. Contour lines of $J_2 = 0$ in the α-ϵ plane, the black solid lines are $A = 0$, $C_b = 0$, $C_0 = 0$, $C_t = 0$. (a) Red dashed line, $A = 0.01$; blue dashed-dotted line, $A = 0.02$; green long dashed line, $A = 0.03$. The other parameters are $C_b = 0$, $C_0 = 0$, $C_t = 0$. (b) Red dashed line, $C_b = 2$; blue dashed-dotted line, $C_b = 4$; green long dashed line, $C_b = 6$. The other parameters are $A = 0$, $C_0 = 0$, $C_t = 0$. (c) Red dashed line, $C_0 = 0$; blue dashed-dotted line, $C_0 = 2$; green long dashed line, $C_0 = 4$. The other parameters are $A = 0$, $C_b = 1$, $C_t = 0$. (d) Red dashed line, $C_t = 0.1$; blue dashed-dotted line, $C_t = 0.2$. The other parameters are $A = 0$, $C_b = 0$, $C_0 = 0$.

where c is the wave speed, which is fixed by imposing the constant volume of fluid condition [14,15],

$$\frac{1}{L}\int_{-L/2}^{L/2} R^2 d\xi = 1. \tag{50}$$

Here, L is the computational domain size, which is also the wavelength of the traveling wave. We use a Fourier spectral method to solve Eq. (49), and a detailed numerical method can be found in the study by Ding and Willis [14]. The one-hump traveling-wave solution is sought from the primary bifurcation of the base state, which is the focus of this section. Other families of traveling-wave solutions can also be found, e.g., period-doubling bifurcation and symmetry-breaking solutions (see Ref. [14]), which will not be explored. The initial guess is drawn from the weakly nonlinear analysis, and branch continuation is implemented for solution tracking as the parameters vary. First, we examine the bending rigidity's effect on the fully nonlinear solutions. Figure 6(a) shows that the bending rigidity promotes the wave speed of the short wave, but it reduces the wave speed of the long wave. Near the primary bifurcation point, as C_b increases, the nonlinear solution branch bends from the subcritical region to the supercritical region, which agrees well with the weakly nonlinear analysis [see also Fig. 6(b)]. Figure 6(b) shows that the droplet size reduces as the surface becomes more rigid [a clearer picture is provided in Fig. 6(d)], which agrees well with the linear stability analysis that the bending rigidity plays a stabilizing effect. Previous studies indicated that larger droplets move faster than small droplets. As a result, the bending rigidity causes a slower moving droplet [see Figs. 6(a) and 6(c)]. The spontaneous curvature plays a similar role to the bending rigidity (see Fig. 7), since it is paired with the bending rigidity. Unlike the spontaneous curvature, the Gaussian curvature plays a different role. The results of traveling-wave solutions shown in Fig. 8 demonstrate that, in the long-wave regimes, the wave speed and height are promoted by the saddle-splay modulus, which agrees well with the linear stability that the Gaussian curvature plays a destabilizing role.

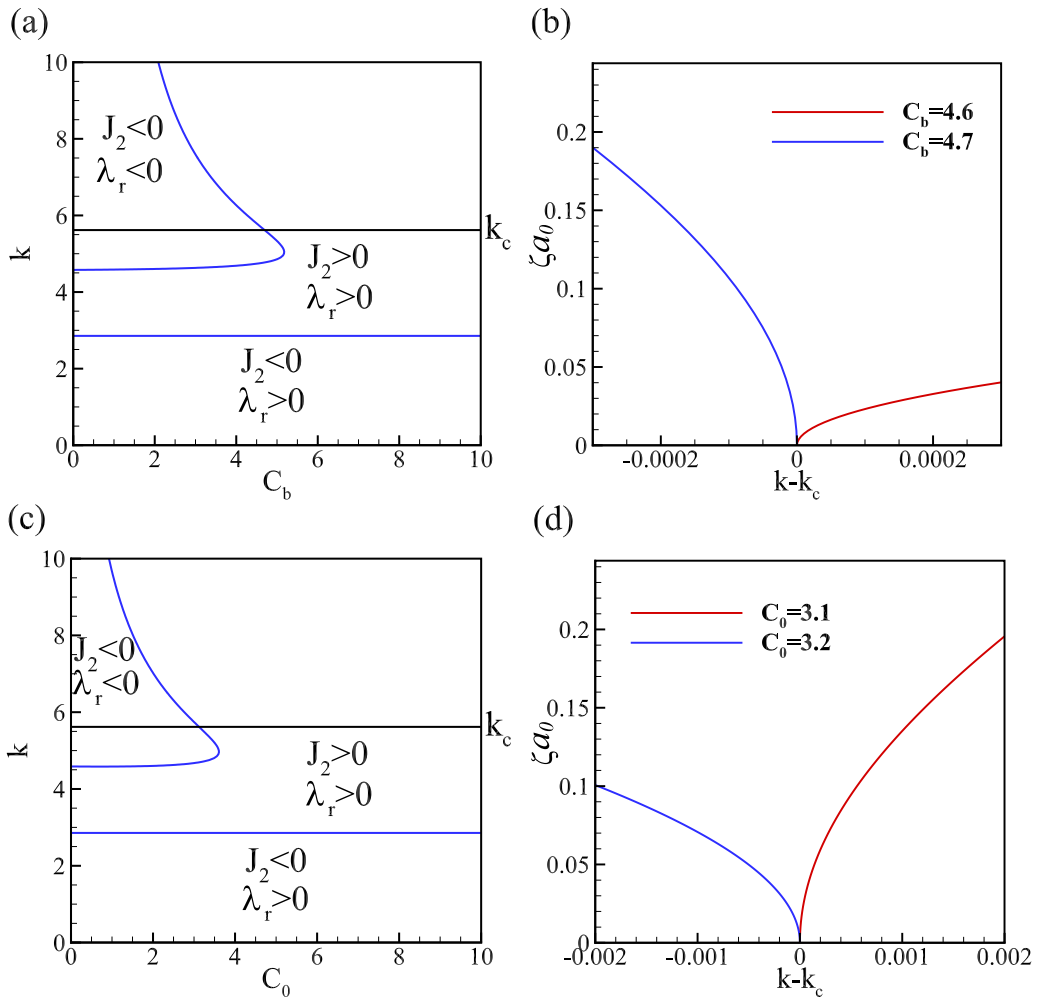

FIG. 5. (a) Neutral stability curve of liquid film for $\epsilon = 0.178$, $\alpha = 0.3262$, $A = 0$, $C_0 = 0$, $C_t = 0$. (b) Subcritical to supercritical change with the increase of C_b. (c) Neutral stability curve of liquid film for $\epsilon = 0.178$, $\alpha = 0.3262$, $A = 0$, $C_b = 1$, $C_t = 0$. (d) Subcritical to supercritical change with the increase of C_0.

Finally, the influence of Van der Waals attractions on the nonlinear solutions is explored (see Fig. 9). By fixing the domain size, we found that the one-hump traveling-wave solutions do not exist when the Van der Waals attractions exceed a critical value, which is marked by the turning point on the curve. The upper branch solution will lose stability to an oscillatory mode, and small-sized beads will emerge [14] (see Appendix B). The interaction between the small beads and the large drop will cause the rupture of the film. The lower branch solution is also unstable, which quickly breaks up into discrete droplets without small-sized beads. An interesting phenomenon observed is that the critical value A_c increases as the domain size L becomes larger. As the wavelength increases, the droplet is larger and moving faster. Thus, the viscous shear stress becomes stronger, which can prevent the breakup of the film. Such a phenomenon has also been reported in liquid jets [38]. We also observed that A_c is promoted by the bending rigidity and spontaneous curvature effect, which, however, is reduced by the Gaussian curvature effect. These results imply that the bending rigidity and the spontaneous curvature effect can retard the breakup of the interface, but the Gaussian curvature effect will accelerate the breakup of the film. Nevertheless, it is not clear how a uniform interface responds to small disturbances, e.g., does it evolve into a stable traveling-wave solution or break up due to the Van der Waals attractions, and how does the surface elasticity affect the evolution process of a uniform interface?

VII. NUMERICAL SIMULATION

This section aims to provide insights into the nonlinear dynamical evolution of a uniform interface subjected to small finite disturbances. We perturb the interface by a harmonic wave:

$$R(z, 0) = 1 + \delta \sin\left(\frac{2\pi z}{L}\right), \quad \delta = 0.2. \tag{51}$$

Equation (21) subjected to periodic boundary conditions was solved numerically using a Fourier spectral method. The solution of $R(z, t)$ is expanded by the Fourier series:

$$R(z, t) = \sum_{-N/2}^{N/2} \hat{R}_n(t) \exp\left(i\frac{2\pi nz}{L}\right), \tag{52}$$

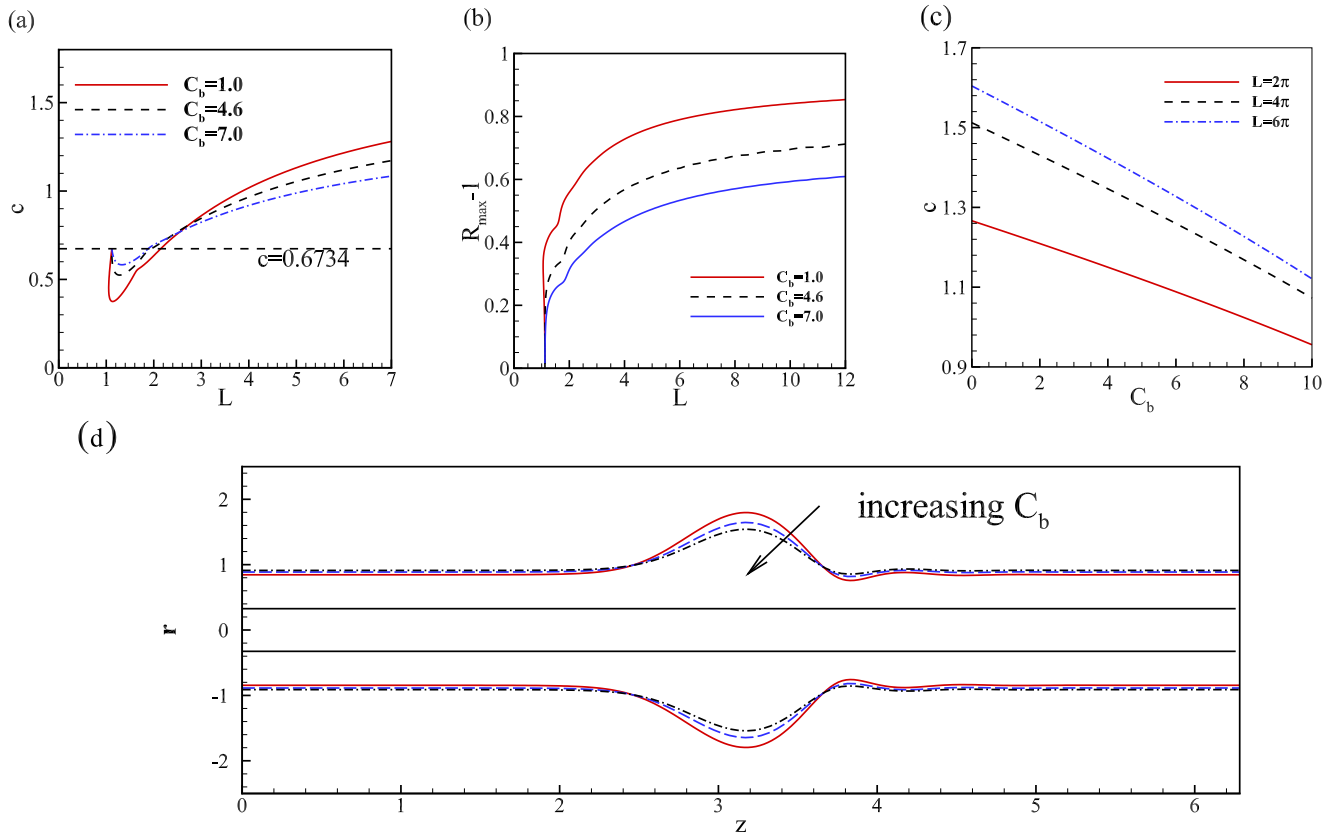

FIG. 6. (a) The wavelength L vs wave speed c with difference bending rigidity C_b. (b) The wavelength L vs maximum film thickness $R_{\max}$ with difference bending rigidity C_b. (c) Bending rigidity C_b vs wave speed c with difference wavelength L. (d) The shape of liquid with different $C_b = 1$ (red solid line), $C_b = 4.6$ (blue dashed line), and $C_b = 7$ (black dashed-dotted line). The other parameters are $\alpha = 0.3262$, $\epsilon = 0.178$, $A = 0$, $C_0 = 0$, and $C_t = 0$.

in which N is the number of Fourier modes, $\hat{R}_n(t)$ is the time-dependent coefficient, and L is the computational domain size. In this section, we used $N = 256$ Fourier modes, which provide sufficient numerical accuracy. We employed an implicit Gear's method for the time stepping, and the relative error is 10^{-6} at each time step [14]. Figure 10(a) displays a typical shape of the liquid film before breakup at $A = 0.05$. Figure 10(b) shows that the film breaks more quickly when the Van der Waals attractions become stronger, which also shows that the minimal thickness reduces exponentially before rupture. To understand the breakup process, a self-similar transformation is used to extract the underlying scaling law [35]:

$$R - \alpha = \Delta t^{\beta} F(\xi), \quad \Delta t = t_r - t, \quad \xi = \frac{z - z_r}{(t_r - t)^{\gamma}}, \tag{53}$$

where t_r is the breakup time and z_r is the breakup location. When the Van der Waals attractions are present, we find that $\beta = 1/5$, $\gamma = 2/5$, i.e., the minimal film thickness reduces as $(t_r - t)^{1/5}$, which is demonstrated in Fig. 10(c). The influence of the curvature elasticity on the breakup process of the film is illustrated in Fig. 11. As expected, the bending rigidity and spontaneous curvature effect retard the breakup of the film, but the Gaussian curvature effect reinforces the breakup of the film, which agrees with the predictions of the linear stability analysis and the traveling-wave solutions. When the Van der Waals force is repulsive, it plays a stabilizing role and prevents the breakup of the film [20]. By starting with the same initial condition, two different flow states were observed by increasing the strength of Van der Waals repulsion, which are illustrated in Figs. 12(b) and 12(c). Figure 12(a) indicates that the flow is steady when the repulsion is weak, but it becomes oscillatory when the repulsion is strong. Such results imply that the steady traveling-wave solutions (which contain two large droplets in a bound state) are not stable attractors, while a time-dependent traveling-wave state (or relative periodic orbit) is stable when the repulsion is strong.

VIII. CONCLUSION

In this paper, we have investigated the dynamics of a liquid film flowing down a microfiber. The effects of Van der Waals attractions and curvature elasticity on the linear stability, weakly nonlinear stability, and fully nonlinear dynamics have been examined using a long-wave model equation. We found that Van der Waals attractions always play a destabilizing effect and Van der Waals repulsions play an adverse role. Unlike the study of an inviscid jet wherein the spontaneous curvature and bending rigidity either stabilize or destabilize the interface due to a wrong expansion of the spontaneous curvature [28], linear stability analysis of the viscous film showed that the spontaneous curvature and the bending rigidity are always

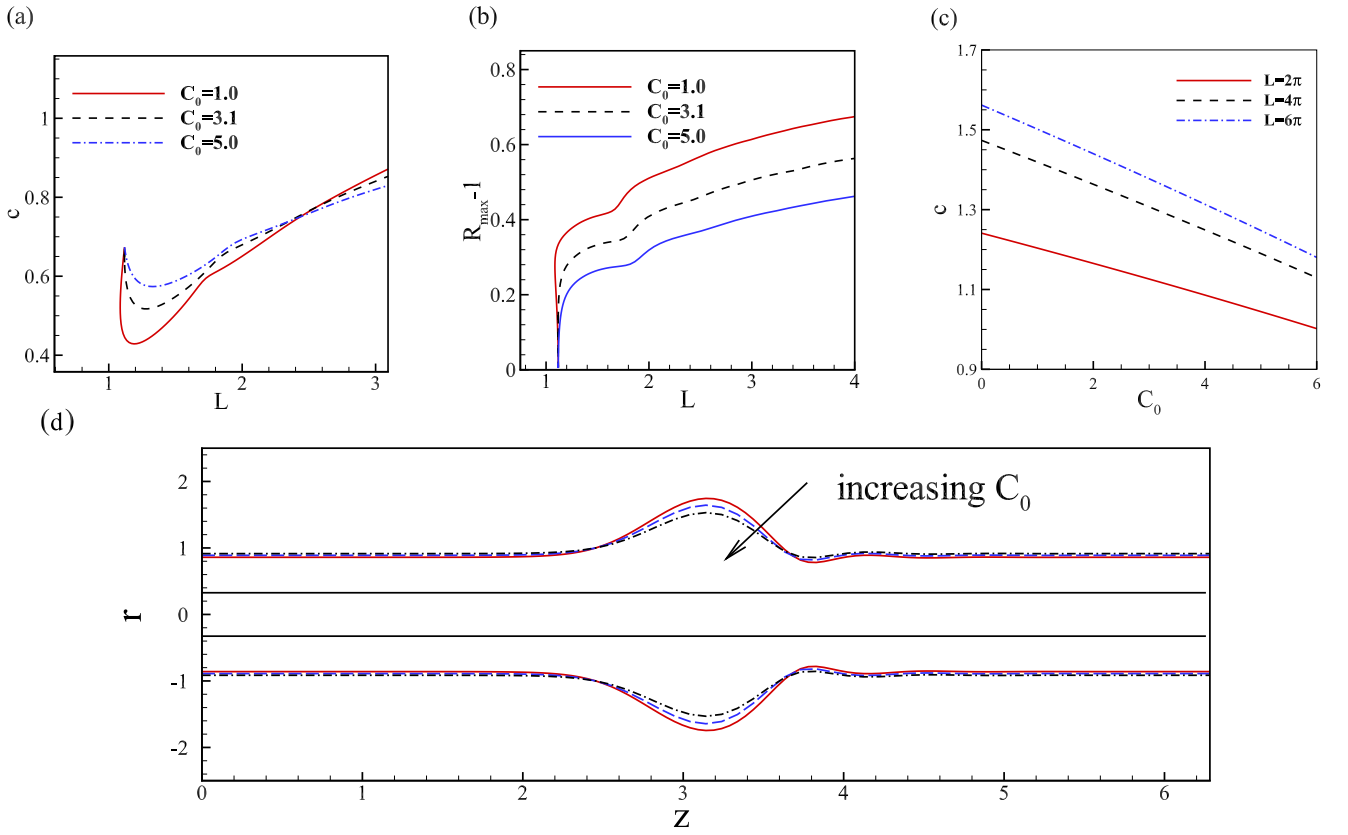

FIG. 7. (a) The spontaneous curvature C_0 vs wave speed c. (b) The wave number k vs maximum film thickness $R_{\max}$ with difference spontaneous curvature C_0. The other dependent parameters are $C_b = 1$, $C_t = 0$, $A = 0$, $\alpha = 0.3262$, and $\epsilon = 0.178$. (c) Spontaneous curvature C_0 vs wave speed c with difference wavelength L. (d) The shape of liquid with different $C_0 = 1$ (red solid line), $C_0 = 3.1$ (blue dashed line), and $C_0 = 5$ (black dashed-dotted line). The other parameters are $\alpha = 0.3262$, $\epsilon = 0.178$, $A = 0$, $C_b = 1$, and $C_t = 0$.

stabilizing. The Gaussian curvature, which was found to be a stabilizing role in the inviscid jet [28], is a destabilizing effect in the viscous film flow due to its tangential component on the liquid interface.

Weakly nonlinear stability analysis showed that the subcritical instability nature of a thick liquid film flow on a thin fiber can transit into supercritical due to the spontaneous curvature and the bending rigidity. The Van der Waals attractions were found to promote the subcritical instability when the fiber is thin, and the supercritical instability when the fiber is thick. But the Gaussian curvature was found to suppress the subcritical instability when the fiber is thin, and the supercritical instability when the fiber is thick.

The primary bifurcation analysis shows good agreement with the weakly nonlinear stability analysis. It demonstrated that the droplet size and moving speed are reduced by the

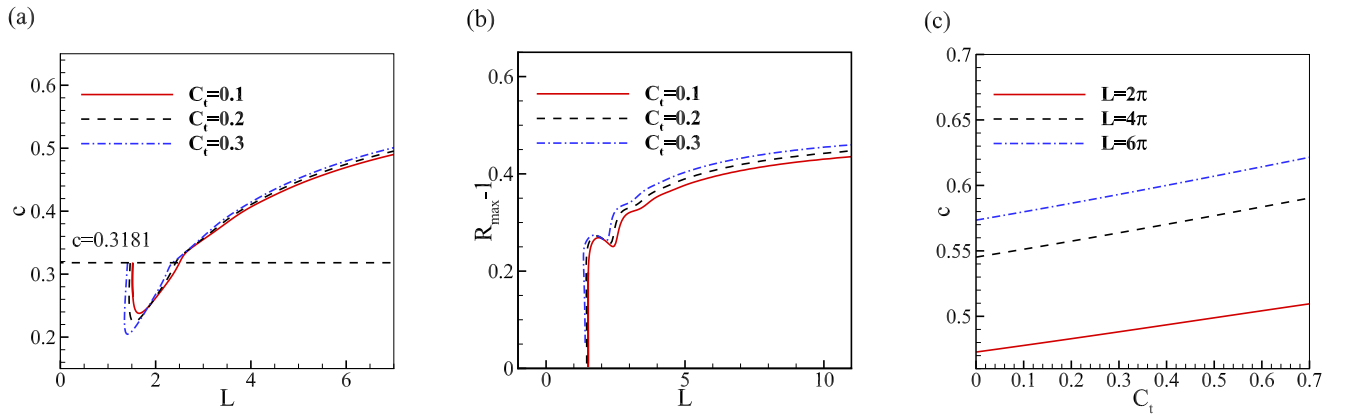

FIG. 8. (a) The wavelength L vs wave speed c with difference saddle-splay modules C_t. (b) The wavelength L vs maximum film thickness $S_{\max}$ with difference saddle-splay modules C_t. (c) Saddle-splay modules C_t vs wave speed c with difference wavelength L. The other dependent parameters are $A = 0$, $C_b = 0$, $C_0 = 0$, $\epsilon = 0.25$, and $\alpha = 0.5$.

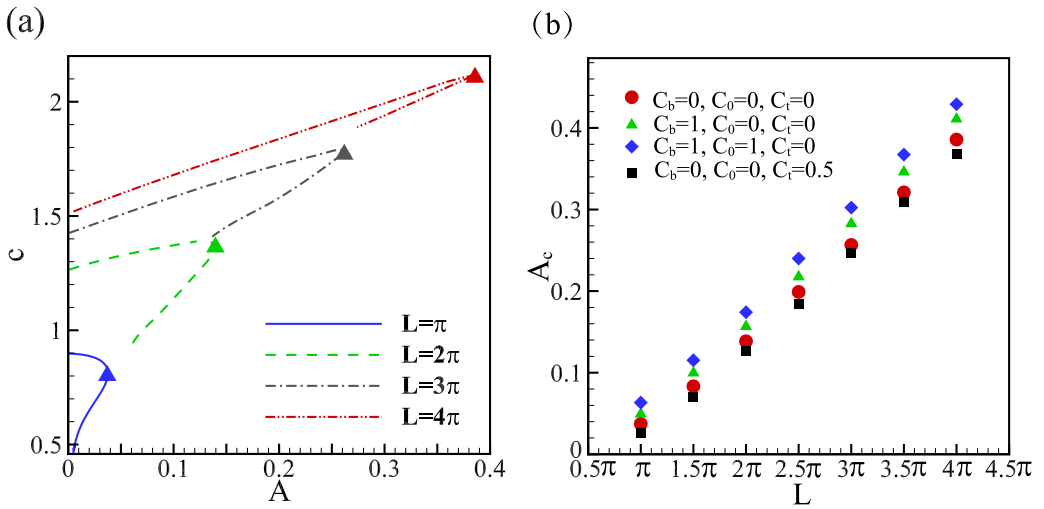

FIG. 9. (a) The wave speed c vs the composite Hamaker number A. Triangles mark the turning points. (b) The critical composite Hamaker number A_c vs the wavelength. The other depending parameters are $\epsilon = 0.178$, $\alpha = 0.3262$.

bending rigidity and the spontaneous curvature, but promoted by the Gaussian curvature. Results showed that the nonlinear traveling-wave solution does not exist when the Van der Waals attractions exceed a critical level, which was believed to be connected with the rupture phenomenon. The bending rigidity and spontaneous curvature can lift up the critical level, while the Gaussian curvature reduces the critical level. Although the nonlinear solutions showed that a larger droplet may move more slowly than a smaller droplet due to the Van der Waals attractions, numerical simulations indicate that these solutions are unstable. Therefore, this counterintuitive phenomenon may not be observable.

Direct numerical simulation demonstrated that the Van der Waals attractions can cause the finite-time breakup of the film, which follows the scaling of $(t_r - t)^{1/5}$ (t_r is the rupture time). The rupture event is postponed by the bending rigidity and the spontaneous curvature, but it is accelerated by the Gaussian curvature. The repulsive Van der Waals force was found to suppress the rupture of film, and increasing the repulsive strength can drive the film to evolve into an oscillatory state rather than a steady state.

ACKNOWLEDGMENTS

The authors are supported by National Natural Science Foundation of China (Grant No. 12102109), and Fundamental Research Funds for the Central Universities (Grants No. AUGA5710000820 and No. AUGA9803504221). Z.D. also acknowledges the warm hospitality of R. Liu when visiting Gui Lin University of Electronic Technology. This work is partially supported by Guangxi Natural Science Foundation (Grant No. 2018GXNSFAA281331).

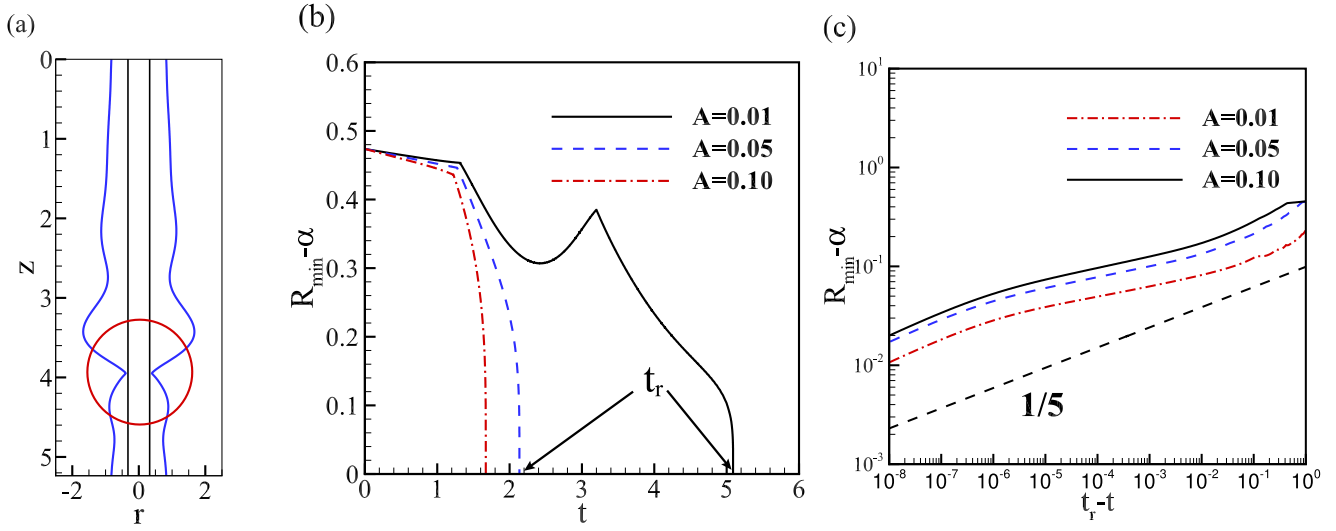

FIG. 10. (a) The instant interfacial shape before breakup. (b) The minimum film thickness vs the evolution time t at different composite Hamaker numbers. (c) The minimal thickness $R_{\min} - \alpha$ vs the time $t_r - t$. The other parameters are $\alpha = 0.3262$, $\epsilon = 0.178$, and $C_0 = C_b = C_t = 0$.

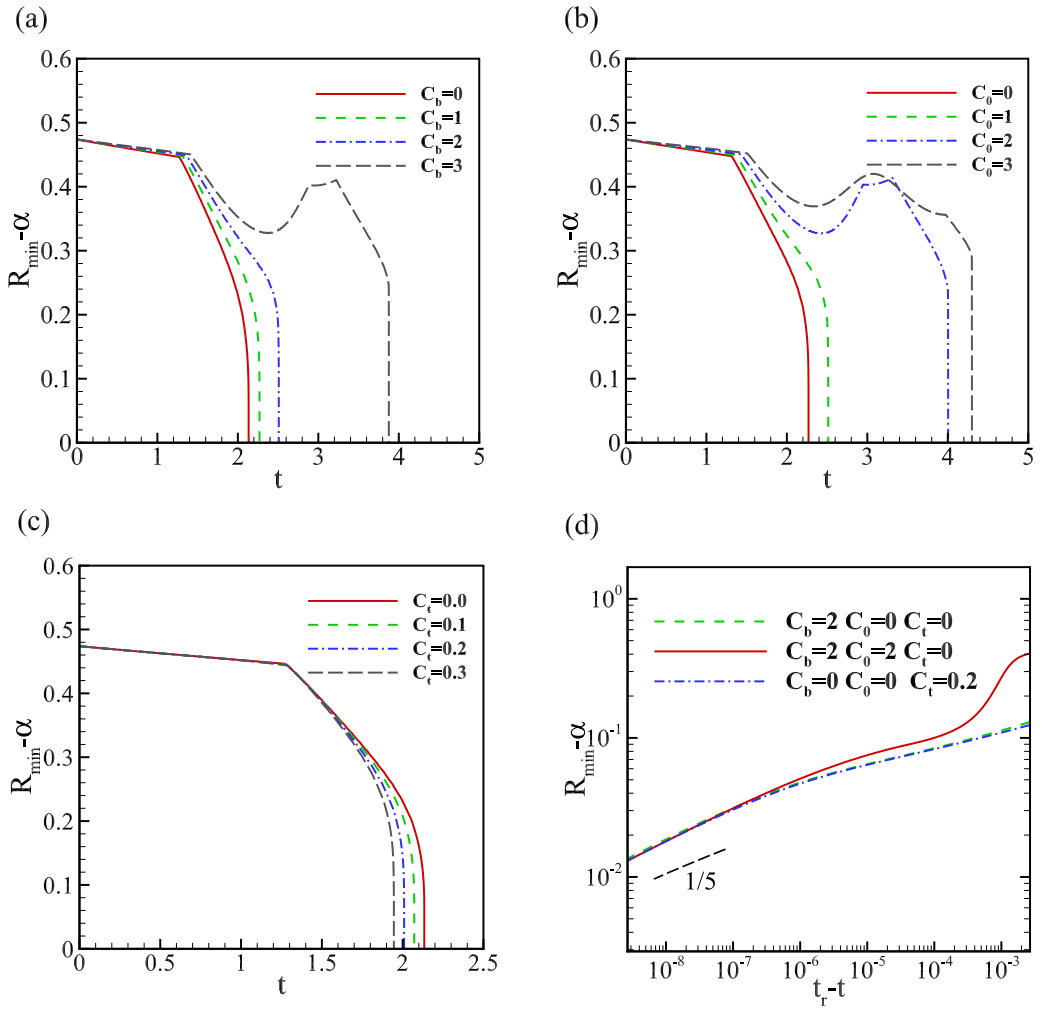

FIG. 11. The change of interface breakup time with bending rigidity, spontaneous curvature, and saddle-splay modulus for $A = 0.05$, $\epsilon = 0.178$, $\alpha = 0.3262$. (a) The other parameters are $C_0 = 0, C_t = 0$. (b) The other parameters are $C_b = 3, C_t = 0$. (c) The other parameters are $C_b = 0, C_0 = 0$. (d) The minimal thickness $R_{\min} - \alpha$ vs the time $t_r - t$.

APPENDIX A: FULLY LINEARIZED PROBLEM

We decompose the (u, w, p, R) into a base state $(\bar{u}, \bar{w}, \bar{p}, \bar{R}) = (0, \frac{1}{4}(\alpha^2 - r^2) + \frac{1}{2}\ln\frac{r}{\alpha}, \text{const}, 1)$ and a perturbed state $(\hat{u}, \hat{w}, \hat{p}, \hat{R})e^{ikz+\omega t}$ wherein the normal mode analysis has been considered:

$$(u, w, p, R) = (\bar{u}, \bar{w}, \bar{p}, 1) + (\hat{u}, \hat{w}, \hat{p}, \hat{R})e^{ikz+\lambda t}. \tag{A1}$$

After linearization, we obtain the following eigenvalue problem in λ:

$$D\hat{u} + \frac{\hat{u}}{r} + ik\hat{w} = 0, \tag{A2}$$

$$\epsilon^4 La(\lambda\hat{u} + ik\bar{w}\hat{u}) = -D\hat{p} + \epsilon^2\left(D^2\hat{u} + \frac{D\hat{u}}{r} - \frac{\hat{u}}{r^2} - \epsilon^2 k^2\hat{u}\right), \tag{A3}$$

$$\epsilon^2 La(\lambda\hat{w} + D\bar{w}\hat{u} + ik\bar{w}\hat{w}) = -ik\hat{p} + \left(D^2\hat{w} + \frac{D\hat{w}}{r} - \epsilon^2 k^2\hat{w}\right), \tag{A4}$$

where $D = d/dr$.

At the fiber interface $r = \alpha$, the boundary conditions are

$$\hat{u} = \hat{w} = 0. \tag{A5}$$

And at the liquid surface, the linearized boundary conditions are

$$\hat{p} = -\frac{3\epsilon A\hat{R}}{(1-\alpha)^4} + (-1 + \epsilon^2 k^2)\hat{R} + \epsilon C_b C_0(-1 + \epsilon^2 k^2)\hat{R} + \epsilon^3 k^2 C_t\hat{R} + \frac{3\epsilon C_b}{8}(\epsilon^2 k^2 - 1)\hat{R} + 2\epsilon^2(D\hat{u} - ikD\bar{w}\hat{R}), \tag{A6}$$

$$D\hat{w} + ik\epsilon^2\hat{u} = \frac{-C_b C_0}{2}(-ik^3\epsilon^3\hat{R} + ik\epsilon\hat{R}) + ik^3\epsilon^3 C_t\hat{R} - \frac{C_b}{4}(-ik^3\epsilon^3\hat{R} + ik\epsilon\hat{R}), \tag{A7}$$

$$\lambda\hat{R} + ik\bar{w}\hat{R} - \hat{u} = 0. \tag{A8}$$

The fully linearized problem is solved using a Chebyshev collocation method [6].

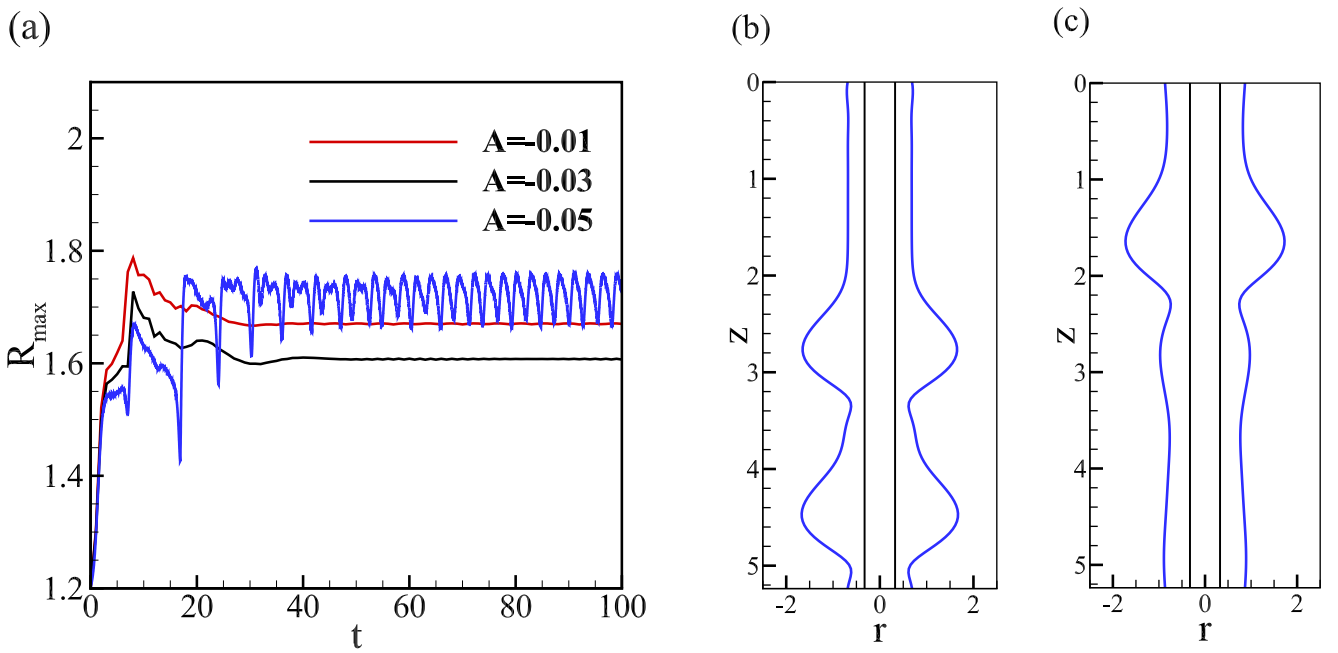

FIG. 12. (a) The maximum thickness $R_{\max}$ vs the evolution time t. (b) Steady state with two droplets at $A = -0.01$. (c) Oscillatory state with one large droplet and a tiny droplet at $A = -0.05$. The other dependent parameters are $C_b = 0$, $C_0 = 0$, $C_t = 0$, $\alpha = 0.3262$, $\epsilon = 0.178$, and $L = 5\pi/3$.

APPENDIX B: NONLINEAR EVOLUTION—STARTING FROM A TRAVELING-WAVE SOLUTION

We examine how the solution evolves from an initial condition of the traveling-wave solution perturbed by small pseudorandom disturbances, such that the stability of the solution on the upper branch and the lower branch can be assessed. For illustration purposes, we fix the domain size at $L = \pi$. The results showed that both the upper branch and the lower branch are unstable. However, the upper branch solution loses stability to an oscillatory mode (periodic orbit). The coalescence between the large drop and the small beads will then cause the breakup of the film. The lower branch is very vulnerable to perturbations, and the small capillary wave in front of the large droplet will be quickly attracted to the fiber surface due to the Van der Waals attractions (see Fig. 13). A counterintuitive conclusion is that the larger droplet solution on the lower branch moves slower than the smaller droplet on the upper branch. Nevertheless, both solutions are unstable, thus we will not observe such a phenomenon in experiments of liquid film flows. However, it is not clear if we can observe this interesting scenario in the motion of a single discrete droplet, when the Van der Waals attractions are significant.

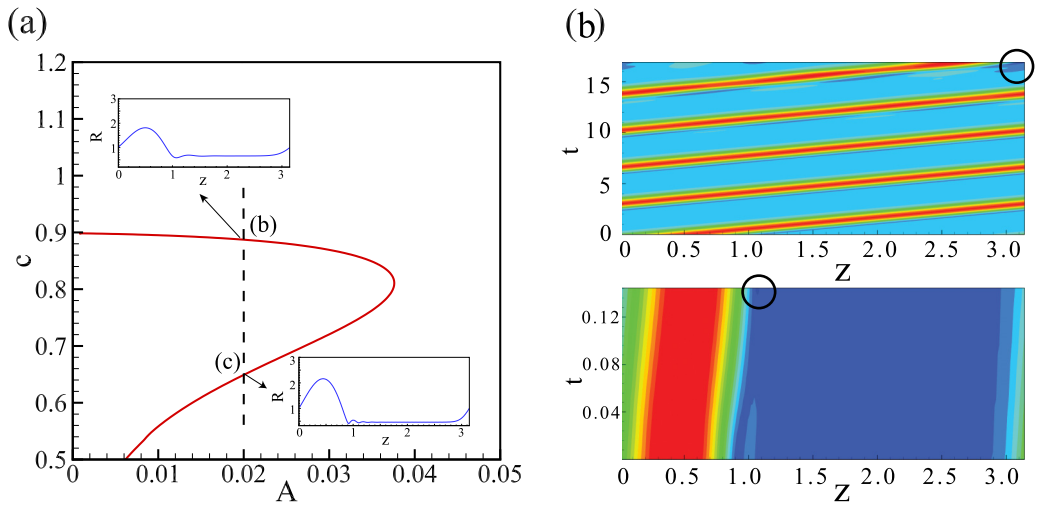

FIG. 13. (a) The traveling-wave speed vs A. The other depending parameters are $L = \pi$, $\alpha = 0.3262$, $\epsilon = 0.178$, $C_b = 0$, $C_0 = 0$, $C_t = 0$. Parts (b) and (c) are selected traveling-wave solutions, which were perturbed by small random disturbances, and the corresponding time evolution is illustrated in the right panel. [(b),(c)] Spatial-temporal diagram of the film thickness $R - \alpha$. The circles mark the rupture events.

[1] J. Ju, Y. Zheng, T. Zhao, R. Fang, and L. Jiang, A multi-structural and multi-functional integrated fog collection system in cactus, Nat. Commun. **3**, 1247 (2012).

[2] A. Sadeghpour, Z. Zeng, H. Ji, N. Dehdari, A. Bertozzi, and Y. S. Ju, Water vapor capturing using an array of traveling liquid beads for desalination and water treatment, Sci. Adv. **5**, eaav7662 (2019).

[3] Y. Tu, C. Liu, C. Chu, H. He, C. Chang, and J. Chen, Bamboo-like nanostructures prepared using template-based wetting methods: molecular arrangements of polyimide and carbon tubes in cylindrical nanopores, Polymer **185**, 121979 (2019).

[4] I. L. Kliakhandler, S. Davis, and S. G. Bankoff, Viscous beads on vertical fibre, J. Fluid Mech. **429**, 381 (2001).

[5] A. W. Wray, D. T. Papageorgiou, and O. K. Matar, Electrified coating flows on vertical fibres: enhancement or suppression of interfacial dynamics, J. Fluid Mech. **735**, 427 (2013).

[6] Z. Ding, J. Xie, T. N. Wong, and R. Liu, Dynamics of liquid films on vertical fibres in a radial electric field, J. Fluid Mech. **752**, 66 (2014).

[7] H. Ji, C. Falcon, E. Sedighi, A. Sadeghpour, Y. S. Ju, and A. Bertozzi, Thermally-driven coalescence in thin liquid film flowing down a fibre, J. Fluid Mech. **916**, A19 (2021).

[8] S. Haefner, M. Benzaquen, O. Bäumchen, T. Salez, R. Peters, J. D. McGraw, K. Jacobs, E. Raphaël, and K. Dalnoki-Veress, Influence of slip on the Plateau-Rayleigh instability on a fibre, Nat. Commun. **6**, 7409 (2015).

[9] D. Quéré, Thin films flowing on vertical fibers, Europhys. Lett. **13**, 721 (2007).

[10] A. L. Frenkel, Nonlinear theory of strongly undulating thin films flowing down vertical cylinders, Europhys. Lett. **18**, 583 (1992).

[11] S. Kalliadasis and H. C. Chang, Drop formation during coating of vertical fibres, J. Fluid Mech. **261**, 135 (1994).

[12] H. C. Chang and E. A. Demekhin, Mechanism for drop formation on a coated vertical fibre, J. Fluid Mech. **380**, 233 (1999).

[13] L. Yu and J. Hinch, The velocity of 'large' viscous drops falling on a coated vertical fibre, J. Fluid Mech. **737**, 232 (2013).

[14] Z. Ding and A. P. Willis, Relative periodic solutions in conducting liquid films flowing down vertical fibres, J. Fluid Mech. **873**, 835 (2019).

[15] R. V. Craster and O. K. Matar, On viscous beads flowing down a vertical fibre, J. Fluid Mech. **553**, 85 (2006).

[16] V. Ya. Shkadov, A. Beloglazkin, and S. Gerasimov, Solitary waves in a viscous liquid film flowing down a thin vertical cylinder, Moscow Univ. Mech. Bull. **63**, 122 (2008).

[17] C. Ruyer-Quil, P. Treveleyan, F. Giorgiutti-Dauphiné, C. Duprat, and S. Kalliadasis, Modelling film flows down a fibre, J. Fluid Mech. **603**, 431 (2008).

[18] E. Novbari and A. Oron, Energy integral method model for the nonlinear dynamics of an axisymmetric thin liquid film falling on a vertical cylinder, Phys. Fluids **21**, 062107 (2009).

[19] A. Sadeghpour, Z. Zeng, and Y. S. Ju, Effects of nozzle geometry on the fluid dynamics of thin liquid films flowing down vertical strings in the Rayleigh-Plateau regime, Langmuir **33**, 6292 (2017).

[20] H. Ji, A. Sadeghpour, Y. S. Ju, and A. L. Bertozzi, Modelling film flows down a fibre influenced by nozzle geometry, J. Fluid Mech. **901**, R6 (2020).

[21] T. Squires, and S. Quake, Microfluidics: Fluid physics at the nanoliter scale, Rev. Mod. Phys. **77**, 977 (2005).

[22] W. Helfrich, Elastic properties of lipid bilayers: theory and possible experiments, Zeitschrift für Naturforschung c **28**, 693 (1973).

[23] Y. Tan, Y. Jin, P. Zhao, J. Wu, and Z. Ren, Lipid droplets contribute myogenic differentiation in C2C12 by promoting the remodeling of the acstin-filament, Cell Death Dis **12**, 1102 (2021).

[24] J. Yang, X. Wen, X. Zhang, X. Hu, L. Fan, D. Jia, Q. Xu, F. Fu, H. Diao, and X. Liu, A lipid coating on cotton fibers with enhanced adsorption capability for fabric functionalization, Cellulose **28**, 5957 (2021).

[25] J. W. Gibbs, The collected works of J. Willard Gibbs. No. 536.7092 (Yale Univ. Press, 1948).

[26] R. C. Tolman, The effect of droplet size on surface tension, J. Chem. Phys. **17**, 118 (1949).

[27] L. Sagis, Generalized curvature expansion for the surface internal energy, Physica A **246**, 591 (1997).

[28] C. Patrascu and C. Balan, The effect of curvature elasticity on Rayleigh-Plateau instability, Eur. J. Mech.-B/Fluids **80**, 167 (2019).

[29] M. K. Dymond, Lipid monolayer spontaneous curvatures: A collection of published values, Chem. Phys. Lipids **239**, 105117 (2021).

[30] R. M. Servuss, W. Harbich, and W. Helfrich, Measurement of the curvature-elastic modulus of egg lecithin bilayers, BBA-Biomembranes **436**, 900 (1976).

[31] Z. S. Davidson, L. Kang, J. Jeong, T. Still, P. J. Collings, T. C. Lubensky, and A. G. Yodh, Chiral structures and defects of lyotropic chromonic liquid crystals induced by saddle-splay elasticity, Phys. Rev. E **91**, 050501(R) (2015).

[32] R. D. Polak, G. P. Crawford, B. C. Kostival, J. W. Doane, and S. Z˘umer, Optical determination of the saddle-splay elastic constant K_{24} in nematic liquid crystals, Phys. Rev. E **49**, R978 (1994).

[33] E. M. Blokhuis and D. Bedeaux, Microscopic theories of curved liquid surfaces, Heterogeneous Chem. Rev. **1**, 55 (1994).

[34] S. A. Safran, Curvature elasticity of thin films, Adv. Phys. **48**, 395 (1999).

[35] Z. Ding, Z. Liu, R. Liu, and C. Yang, Breakup of ultra-thin liquid films on vertical fiber enhanced by Marangoni effect, Chem. Eng. Sci. **199**, 342 (2019).

[36] A. Oron, S. H. Davis, and S. G. Bankoff, Long-scale evolution of thin liquid films, Rev. Modern Phys. **69**, 931 (1997).

[37] C. I. Chen, C. K. Chen, and Y. T. Yang, Weakly nonlinear stability analysis of thin viscoelastic film flowing down on the outer surface of a rotating vertical cylinder, Int. J. Eng. Sci. **41**, 1313 (2003).

[38] J. Eggers and M. A. Fontelos, *Singularities: Formation, Structure, and Propagation* (Cambridge University Press, Cambridge, 2015).